Structural Behavior of Large-Scale I-Beams with Combined Textile and CFRP Reinforcement

Jan Bielak [1,*] **, Maximilian Schmidt** [1] **, Josef Hegger** [1] **and Frank Jesse** [2]

[1] Institute of Structural Concrete, RWTH Aachen University, 52074 Aachen, Germany; mschmidt@imb.rwth-aachen.de (M.S.); jhegger@imb.rwth-aachen.de (J.H.)

[2] Hentschke Bau GmbH, 02625 Bautzen, Germany; Jesse.Frank@hentschke-bau.de

* Correspondence: jbielak@imb.rwth-aachen.de; Tel.: +49-241-80-26830

check for updates

Abstract: With the innovative composite material carbon-reinforced concrete, thin-walled, high-performance components can be realized. A combination of carbon fiber reinforced polymer (CFRP) bars and non-metallic textile grids is advantageous as it exploits the full potential of the high-performance materials to reduce dead loads, increases durability, and extends lifespan. For new components with such mixed reinforcement, applicable design concepts and engineering rules are necessary to accurately determine the structural and deformation behavior. To validate models and detailing rules previously developed, three large carbon reinforced concrete I-beams were designed and tested to failure with a realistic line load. CFRP bars served as principal bending reinforcement, whereas shear and flange reinforcement consisted of textile grids. Results showed that existing models for bending using variation of strain distribution as well as non-linear finite-element analysis predicted the flexural behavior of structural components with mixed reinforcement in ultimate limit state (ULS) appropriately. Yet, calculation of shear capacity requires further studies to determine textile reinforcement contribution and estimate reduction for concrete strength in reinforced compression struts. For serviceability limit state (SLS), three methods for determination of deflection delivered good results. In future, a rethinking is required with regard to the ductility and robustness of CFRP-reinforced concrete components. In this respect, pronounced cracking as well as the large ultimate strain and deflection compensate for the lacking yield capacity of the reinforcement.

Keywords: textile-reinforced concrete; carbon reinforced concrete; continuous load; finite-element calculation

1. Introduction

Global mega trends such as climate change, growth of population with further urbanization, and increase of land consumption as well as further increase in mobility require great efforts from society in general and the construction sector in particular. Construction industries world-wide will struggle to meet the demands of those mega trends with established methods and incremental innovations thereof. Completely new approaches and radical innovations are called for. Carbon concrete composites or carbon reinforced concrete (CRC) and textile reinforced concrete (TRC) qualify as such disruptive innovations [1], which are atypical for the building sector. Indeed, using those materials enables a complete rethinking of established construction strategies [2–5]. The higher tensile strength of reinforcement fibers such as carbon compared to typical reinforcement steel, combined with the complete insensitivity to corrosion, allows for optimization of cross-sectional designs. Often, the potential of reduction of CO_2-consumption by use of CRC in new structural components is highlighted [6,7]. This is said to be achieved through reduction of concrete mass (and especially cementitious binder) by minimization of concrete cover, member web thickness, and consequently dead load. Here, the idea

of merely replacing steel reinforcement is prevalent. Equally important is the extension of lifespan of new concrete components which is enabled by better durability of the reinforcement materials [8], especially in environments with severe exposition. The same reasoning applies for strengthening of existing structures with non-metallic reinforcement [9,10]. By extending lifespan, the embodied CO_2 in concrete parts can be spread over a longer period of use, and furthermore, cost-efficiency increases. Decrease of life-cycle cost for certain applications through use of non-metallic reinforcement (see for example [11,12]) might be the most convincing argument for most stakeholders in construction. This is typically the case when maintenance-intensive additional polymeric coatings are no longer needed [13–15].

Despite those advantages, market share of non-metallic reinforcement is still negligible, and thus the potential effect on consumption of resources is limited. One explanation next to higher initial investment costs for production of elements [16] might be the shortfall of a comprehensive set of design models and standardized test procedures based on fundamental research. World-wide, first building codes were established for use of fiber reinforced polymer (FRP) reinforcement [17–19], but in Europe, an implementation is still pending. Even then, design rules might be insufficient: New construction strategies really exploiting the potential of thin, non-metallic reinforced membranes are lacking. Instead, engineers try to keep conventional principles and cross-sections, just replacing the steel.

The C^3-initiative [20], a large-scale coordinated research program in Germany, examines various facets of the topic in depth: Fundamental research, potential applications, and market penetration. This study presents results from the final stage of this project, focusing on engineering models, design approaches and standardization of test methods for CRC constructions. With experimental and subsequent numerical investigations of large-scale I-beams, verification of approaches to design and calculation of members with mixed carbon fiber reinforced polymer (CFRP) reinforcement in serviceability limit state (SLS) and ultimate limit state (ULS) is possible. We should mention that the idea of combining (different) textiles and FRP-bars is not new. Previous application examples from practice are facades [21,22], pedestrian bridges [23,24], or precast elements [25]. Kromoser et al. conducted studies on slender I-beams with mixed reinforcement [3]. Kueres [24,26] investigated beams with CFRP prestressing strands and textile shear reinforcement. May et al. investigated ceiling systems with CFRP bars and textile grids [4]. Schumann et al. tested I-beams with Glass-FRP longitudinal bars and carbon textile shear reinforcement [27]. Chudoba et al. performed numerical investigations of members containing different textiles [28]. So far, a systematic investigation of the effect of loading with line loads, the focus on specific deflection configurations in SLS and chosen failure mechanisms in ULS, and the influence of cross-sectional slenderness and large (and realistic) scale of the beams has not been not investigated. The latter is of importance for detailing, as several aspects of load-bearing behavior relate to scale. For example, providing sufficient anchorage length of textile shear reinforcement is more difficult for beams with smaller effective depth [29–31]. Also, bond failure of longitudinal reinforcement might be more relevant for beams with less anchorage length at the supports. Downscaled tests might prove inapt to investigate those aspects.

The main research questions addressed in this paper can be summarized to:

- Are existing calculation models for bending capacity using material characteristics from component tests applicable to members with mixed CFRP rebar and textile reinforcement?
- Can the strength of non-prestressed carbon bars and of carbon textiles fully exploited at SLS and ULS?
- Can detailing rules be transferred from steel reinforced concrete members?
- Are predictions of deflection with existing models (for example [32]) possible?

First, the materials and methods used in experimental and numerical investigations of three beams are presented. Then, the presentation of the experimental and numerical results enables a detailed discussion. The paper finishes with concluding remarks.

2. Experimental Investigation: Materials and Methods

2.1. Reinforcement

For the experimental part in this study, various non-metallic reinforcement types were combined to make use of their individual strengths. The main reinforcement in the tension flange of the I-shaped beams was a non-prestressed CFRP rebar (Figure 1c, and Table 2) with milled helix ribs. As shear reinforcement, an epoxy-impregnated biaxial carbon grid was utilized. This type of reinforcement is pre-impregnated and pre-hardened by the manufacturer. Figure 1a shows the open structure of the symmetrical reinforcement with a 38 mm axial spacing of the yarns in both directions. Pre-formed textile grids made of CFRP (Figure 1b) or alkali-resistant (AR-) glass (GFRP) served as reinforcement of the flanges. Both had the same mesh geometry as the planar shear reinforcement.

| (a) | (b) | (c) |
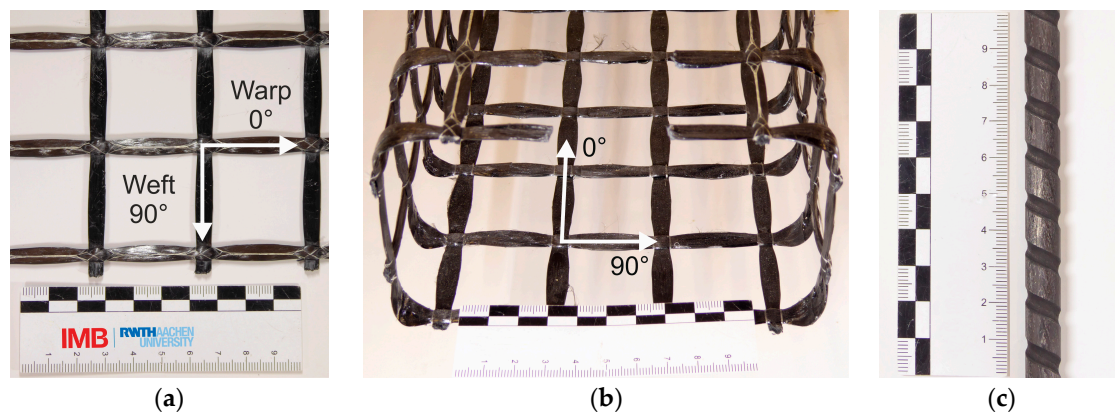
Figure 1. Reinforcement types: (**a**) Planar biaxial carbon fiber reinforced polymer (CFRP) grid; (**b**) pre-formed CFRP grid; (**c**) CFRP rebar with milled ribs.

As the yarns were fully impregnated, a homogeneous stress distribution over the cross-section with full activation of all filaments can be assumed, while non-impregnated "dry" yarns would exhibit different behavior, with telescopic failure and inhomogeneous stress distribution [33]. Thus, in the present case, material characteristics (strength, modulus of elasticity) can be tested on individual yarns extracted from the grid without surrounding concrete [34]. Key properties are listed in Table 1. The ultimate stress and modulus of elasticity were analyzed in uniaxial tension tests on individual yarns according to the setup described in [35]. It should be highlighted that, due to the well-known statistical effects for a bundle of linear-elastic yarns with brittle failure, the strength of an individual yarn underestimates the strength of the fabric [36,37]. For the textile reinforcement in this study, Rempel proposes a reduction factor of 0.85 [34,38] for n -> ∞ yarns. The bond properties of the textile reinforcement were analyzed in a previous study [39,40]. The complete epoxy impregnation enables form closure with splitting of the concrete as primary bond mechanism. This is different from non- or incompletely impregnated textiles with failure mechanisms such as pull-out and jamming of the yarns [41]. The bond strength is highly dependent on local yarn geometry. Resulting from the production process of the pre-formed grids, individual filaments are less straight than in planar grids. This results in a higher waviness, as can be seen in Figure 1a,b. As a consequence, higher form closure and higher tendency for splitting [42–44] occur.

Table 1. Reinforcement characteristics for impregnated planar carbon and alkali resistant (AR)-glass grid (properties of one individual yarn, from [34] with test setup according to [35]).

Characteristic	Unit	Carbon [*]		AR-Glass [*]	
		(0°)	(90°)	(0°)	(90°)
Modulus of elasticity	[MPa]	244,835	243,828	70,843	74,618
Mean ultimate stress	[MPa]	3221 (n = 204) [†]	3334 (n = 218) [†]	1590 (n = 448) [†]	1599 (n = 477) [†]

Table 1. *Cont.*

Characteristic	Unit	Carbon [*]		AR-Glass [*]	
		(0°)	(90°)	(0°)	(90°)
5% quantile ultimate stress	[MPa]	2737	2762	1363	1372
Mean ultimate strain	[‰]	13.2	13.7	22.4	21.4
Axial spacing of yarns	[mm]	38	38	38	38
Cross-sectional area per yarn [‡]	[mm²]	3.62	3.62	4.62	4.62
Cross-sectional area per meter [‡]	[mm²/m]	95	95	121	121

[*] Values for planar material. Tensile characteristics of pre-formed grids may differ. [†] Number of tests. [‡] Filament cross-sectional area without epoxy-impregnation.

In preparation of the large-scale tests, uniaxial tensile tests on the main CFRP rebar were conducted to verify the manufacturer's specifications. While test procedures for FRP elements exist (e.g., [45,46]), they were typically developed for glass-fiber reinforced polymer bars. With higher fiber strength, anchorage failure might occur despite longer sleeve length prior to failure in the free length. ASTM D7205 recommends 460 mm sleeve length for a 9.5 mm CFRP bar. More sophisticated clamping devices use inversely segmented cones [47,48] or a pressure gradient. Here, two different test were utilized: A horizontal setup with two hydraulic jacks and a 400 mm concrete anchor block on both sides and a setup with adhesive anchorage using a two component epoxy resin in 150 mm threaded steel sleeves (Figure 2). To reduce the necessary anchorage length and prevent anchorage failure, an inner thread M16 was cut in the sleeve. With both setups, it was possible to achieve failure in free length. Yet, for some specimen of the second setup, failure of the milled ribs (shearing off) at the beginning anchorage was observed.
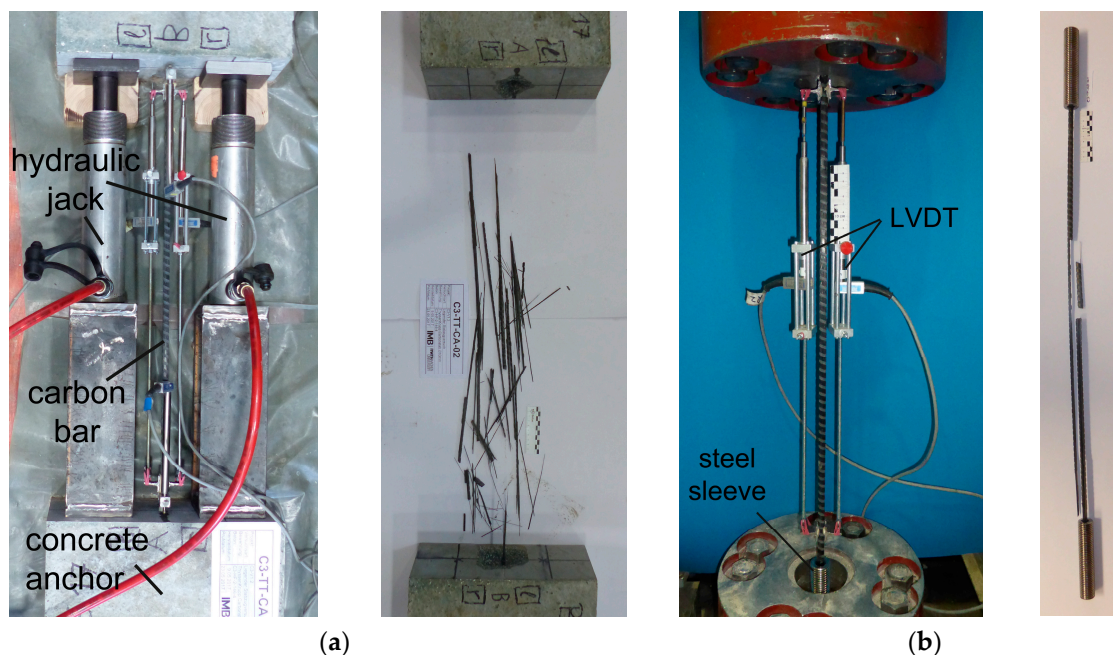
Figure 2. (**a**) Testing of carbon bars in uniaxial tension with concrete anchorage and (**b**) with adhesive anchorage in steel sleeve.

The results of both tests are summarized in Table 2. The difference to the material characteristics given by the manufacturer might result from a different definition of cross-sectional area. For our tests, all stress values relate to the nominal cross-section area of 61.5 mm², corresponding to the measured core diameter of approximately 8.9 mm. As the rebar was still under development during production of the beams, a high variation in material properties from batch to batch has been observed.

Table 2. Reinforcement characteristics for carbon bars.

Characteristic	Unit	Own Tests	Manufacturer [49]
Modulus of elasticity	[MPa]	165,515 *	151,000 [†]
Mean ultimate stress	[MPa]	1828 * (n = 5 tests)	1650 [†]
Mean ultimate strain	[‰]	11.04	10.9
core diameter	[mm]	8.9	8.5
nominal diameter ([50], Annex A)	[mm^2]	9.5	-
outer diameter	[mm^2/m]	10.0	10.0
Mean bond force per embedded length, values from MFPA Leipzig GmbH [51]	[kN/mm]	0.976 (n = 12 tests) [‡]	-

* Reference cross-section area 61.5 mm^2. [†] Reference cross-section area not given by manufacturer, supposedly 56.7 mm^2. [‡] Determined on cubic specimen (age 28 d) according to RILEM-Pull-out [52], embedded length (50, 75 or 100 mm) in the center of the specimen, concrete C3-B2-HF-145-3 with $f_{cm,pris}$ = 111.3 MPa and $f_{ctm,fl}$ = 10.3 MPa.

2.2. Concrete

The concrete utilized in this study (Table 3) was adapted by the manufacturer Hentschke Bau GmbH from a mixture developed within another subproject of C^3 [53]. It meets the requirements of industrial production and is suitable for densely reinforced, thin-walled CRC. The maximum diameter of the crushed aggregate (4 mm) matched the size of the grid openings and rebar spacings. The cementitious binder compound with its optimized fine grain size distribution and the fine sand paired with the high-performance superplasticizer led to self-compacting properties of the fresh mix. However, during production, external vibration was applied to further enhance concrete flow speed and venting.

Due to its small aggregate size and high content of fine particles, the mixture does not qualify as standard concrete according to DIN EN 206 [54]. Yet, the term "concrete" is used within this paper to distinguish its use for new concrete parts clearly from repair and retrofitting applications of TRC, where the term "mortar" is preferred [55,56].

Table 3. Mix design of concrete C3-B2-HF-2-155-5.

Substance	Content
	kg/m^3
Cementitious binder compound CEM II/C-M Deuna	663
Fine quartz sand BCS 413 0.06/0.2 mm	240
Quartz sand Hahnenberg 0–0.2 mm	506
Lengefelder Marmor Saxogran (crushed marble) 2.0–4.0 mm	832
Superplasticizer (polycarboxylatether-basis) MC-VP-16-0205-02	14
Water	145

The material characteristics of the hardened concrete, tested on the same day as the I-beams, are given in Table 4. The bending tensile strength $f_{ctm,fl}$ was determined on prism specimens (40 × 40 × 160 mm), according to the standard test method for mortar [57]. The splitting tensile strength $f_{ct,sp}$ was tested on shortened cylinders (d/h = 150/150 mm, only the lower half was tested). The compressive strength was determined on 150 mm cubes ($f_{cm,cube}$), on cylinders with d/h = 150/300 mm ($f_{cm,cyl}$) according to [58] and prism halves ($f_{cm,pris}$) according to [57]. The mean modulus of elasticity E_{cm} of the cementitious matrix was tested on cylindrical specimens (d/h = 150/300 mm) with method "B" specified in [59]. The compressive strain at maximum load ε_{c1} was determined with external strain gauges glued on one cylinder from each batch.

2.3. Test Setup and Instrumentation

To test the beams with a uniformly distributed load, an inverse setup was employed (Figure 3) [60]. Ten equally spaced hydraulic jacks connected to one hydraulic circuit applied the load to the lower chord

of the beams. A package of steel (300 × 300 × 30 mm) and plywood (t = 21 mm) plates reduced local stress concentrations. Spherical bearings centered the vertical load while curvature of the beams increased during the test. Initial geometrical non-linear finite-element calculations employing a horizontal line-load equivalent to an imperfection of 30 mm in mid-span predicted deformation-induced lateral failure of the beams' compression chord prior to bending failure. Thus, lateral supports in mid-span with polytetrafluorethylene (PTFE) facings were added. All specimens were tested under quasi-static conditions with a load rate of 10 kN/min. At predefined intervals, the test was halted to mark new cracks and document the crack pattern. After reaching a midspan deflection of 28 mm, all beams were completely unloaded and reloaded to identify plastic deformation and remaining crack-openings.

Table 4. Material properties of hardened concrete at the day of testing.

Test No.	Age	$f_{cm,cube}$	$f_{cm,cyl}$	$f_{ct,sp}$	$f_{cm,pris}$	$f_{ctm,fl}$	E_{cm}	ε_{c1}
	[d]	[MPa]	[MPa]	[MPa]	[MPa]	[MPa]	[MPa]	[‰]
FT01	28	112.7	98.8	5.58	95.75	12.29	38,750	2.69
FT02	22	111.0	- *	5.25	94.96	13.42	39,890	- *
FT03	30	104.6	97.0	4.77	97.01	13.23	40,620	2.65

* For numerical calculation, $f_{cm,cyl}$ was converted with the factor 1/1.11 from $f_{cm,cube}$ (Mean conversion of FT01 and FT02) to $f_{cm,cyl}$ = 100.0 MPa. The mean value of ε_{c1} = 2.67‰ was chosen for calculation of FT02.

Vertical displacement (DU1–DU6) was measured at supports, in in mid-span and at two locations in between (Figure 3). Three horizontal linear variable displacement transducers (LVDT) Bi1–Bi3 in the tension zone and nine (eleven for FT02) concrete strain gauges in the compression chord tracked deformations from the exterior. For internal measurement, strain gauges were applied to the main carbon bars. Therefore, one section of a rib was carefully sanded off without damaging the core diameter of the bars and the gauges were glued on the CFRP rebars. The feasibility of this measurement was evaluated in previous uniaxial tensile tests, where strain measurements with conventional LVDTs and strain gauges yielded similar results. For FT01 and FT02, six gauges (D1S–D6S) were fixed at the second and fourth bar of the outermost reinforcement layer (Figures 3 and 4). For FT03, a total of eight gauges were used, four outside of the splice, and four in the first and last third of the splice length.

2.4. Cross-Section and Reinforcement Layout

The dimensions of the cross-section of beams FT01–FT03 (Figure 5) were chosen based on an preliminary design using sectional analysis and a conventional finite-element program [61] designed for steel-reinforced concrete utilizing adapted material parameters. The main design criteria were:

- To investigate the bending behavior at ultimate limit state, especially

  ○ Rupture of tensile reinforcement (FT01)
  ○ Flexural failure of concrete compressive zone (FT02)
  ○ The behavior of a zone with full rebar splice (FT03)

- To prevent unintended failure, e.g., in shear, in anchorage, or in deformation induced failure (for example in lateral failure of the compression chord or in local failure of the web)
- To evaluate sufficient announcement of failure between SLS, defined by the limits of deflection, and ULS for bending
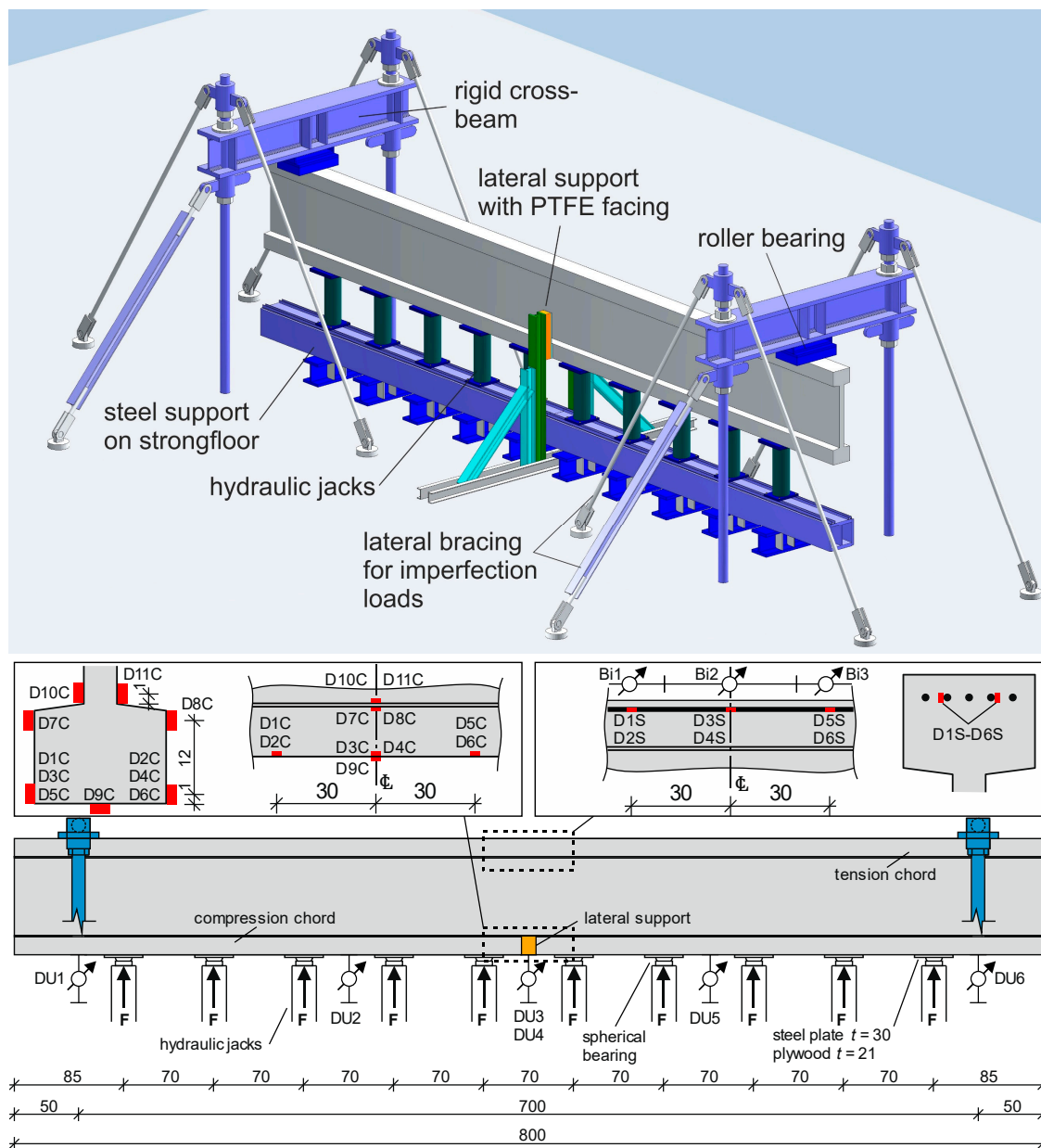
Figure 3. Test setup with continuous loading and instrumentation.

The slenderness of $l/h = 700/90 = 7.8$ resulted from full utilization of the non-prestressed carbon rebars at ULS and complying with SLS requirements for FT01, i.e., deflection limit. No precamber was chosen for the beams. The width of 200 mm for the tension flanges was necessary to place 20 bars of FT02 with adequate spacing. The same width was chosen for the compression flange to increase lateral stiffness. The depth of 150 mm of the tension and compression chords ensured anchorage of the planar shear reinforcement (see e.g., [39] for determination of the full anchorage length in warp direction of 78 mm for a comparable cementitious matrix). However, the compression chord depth for FT02 was reduced in mid-span to diminish the resistance of the compression zone in order to provoke flexural compression failure of concrete. A web width of 50 mm allowed for concreting the beams in upright position with 4 layers of shear reinforcement for FT02. A minimum concrete cover of 10 mm was chosen in the web based on previous experience from uniaxial tensile tests [62]. Previous studies on tensile specimen reinforced with the same carbon rebar indicated that a cover of 25 mm is necessary in the tension zone to transfer bond forces [40] without premature longitudinal cracking and concrete

spalling. The same cover was chosen for the grid in the compression flange. As shown in Figure 5 (left), preformed grids in compression (CFRP grid) and tension flange (GFRP grid) were chosen to take the tension forces resulting from lateral connection of the outlying rebar and concrete areas. The profiles were open to the center of the beam, allowing the primary shear reinforcement to penetrate and securely anchor in the flange. To close the open profiles and to increase the resistance in lateral direction, short carbon bars from the same material as the main rebars were added (see Figure 6). AR-glass fabrics were chosen specifically for the tension flange for their higher ultimate strain (Table 1) to prevent premature rupture of the longitudinal yarns and spalling of the concrete. The lap length of 50 cm was chosen based on bond strength value from Eurocode 2 [63], clause 8.4.2, using mean tensile strength of a C100/115 (f_{ctm} = 5.2 MPa), for ultimate strength of carbon bars (1828 MPa) and the corresponding diameter (8.9 mm). Because of self-compacting concrete properties, good bond conditions were assumed and a factor α_6 = 1.4 was assumed.

Figure 4. Left: Detail of internal strain gauge for carbon bar; **right**: position of strain gauges for FT01 in tension chord.

2.5. Production

The production of the beams in the precast plant utilized conventional formwork and production methods (Figure 6). Textile planar and preformed grids and rebars were combined to a complete reinforcement cage which was equipped with conventional short fiber reinforced concrete spacers at the bottom and at the top to prevent uplift. At the sides, special plastic spacers for textile grids kept the 10 mm concrete cover of the shear reinforcement. The concrete was poured in the formwork slowly by a screw conveyor, aided by mild external vibration. Each beam was demolded after one day and stored under plastic foil until transport to the testing facility. The outstanding surface quality with almost no pores is evidence of good compaction of the concrete despite dense reinforcement.

All beams were stored in statically determined manner until testing, allowing for free deformation. At an age of 2–3 weeks, vertical cracks in beams FT01 and FT02 occurred. The cracking was caused by restraint of drying shrinkage deformation due to high reinforcement ratio in the tension flange (eigen stress). FT01 cracked on a length of 2 m in the center of the beam with 11 cracks, 6 of which running from the top flange through the web and into the bottom flange with crack widths of 0.05 to 0.1 mm and a mean spacing of 12 cm. FT02 exhibited a denser crack pattern (97 cracks) in the highly reinforced tension flange with a mean spacing of 8.1 cm and a mean crack width of 0.1 mm. Seven cracks in midspan over a length of two meters ran into the web, but did not reach the compression flange. FT03 remained uncracked until testing.

3. Methods of Theoretical Investigation

3.1. Design with Spreadsheet Calculation

For bending design, sectional analysis with iterative variation of the linear strain distribution assuming perfect bond was utilized. As stress–strain relation for concrete in compression, the approach according to EC2 [64] was chosen. In addition to the main reinforcement, each longitudinal yarn of

flange and shear reinforcement in the tension zone was considered with its respective contribution. For FT01, the failure criterion was set to reaching the ultimate strain of the main carbon bars, while for FT02 reaching the ultimate compressive strain $\varepsilon_{c1,u}$ was decisive.
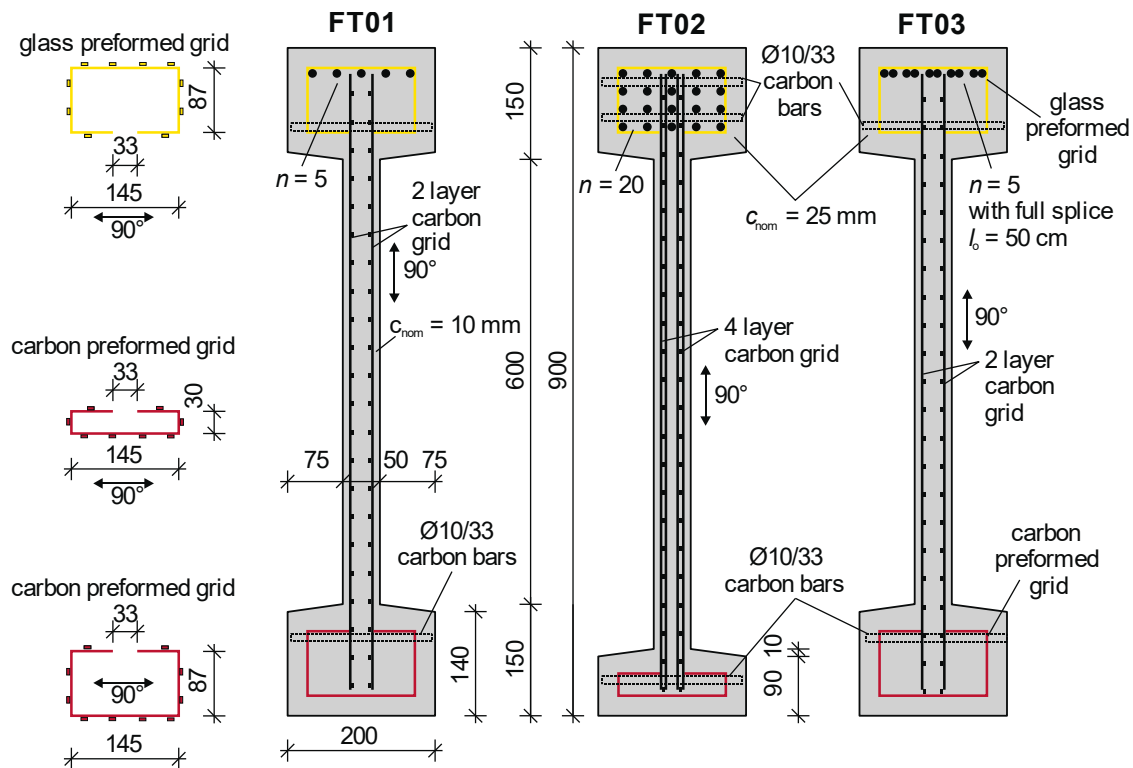

Figure 5. Cross-sections and reinforcement layout of beams FT01–FT03 in mid-span.

The limit of shear resistance was determined with a strut-and-tie model with variable inclination of the compression field from EC2 [64]. While for FT01 with two layers of shear reinforcement a strut inclination of $\cot(\theta) = 2.5$ was chosen, for FT02 with a doubled shear reinforcement a strut inclination of $45°$ was estimated. In both cases the maximum compressive stress of the concrete strut was $\sigma_c = 0.6 \cdot (1 - 100/250) \cdot 100 = 36$ MPa. Strain in shear reinforcement of FT01 did not exceed 2.87‰. Direct loading within distance *d* from the support was not considered in shear verification. The strain in shear reinforcement of FT02 was calculated to 8.3‰, which is lower than the upper limit 9‰ given e.g., by [65].

3.2. Non-Linear Finite Element Approach

ABAQUS/CAE [66] was employed in a refined geometrical and physical non-linear FE analysis. Key input parameters are given in Figure 7. For simple bending analysis, a 2D-modelling approach would have been sufficient and computationally much more efficient. Beams FT01 and FT02 were modeled in 3D using symmetry conditions to be able to account for global stability (lateral deformation-induced failure of compression chord) and local stability (deformation-induced failure of the web in compression). For textile reinforced concrete, often a smeared approach to modeling reinforcement is chosen (see for example [67]). Here, all tension reinforcement is modeled discretely, using two node truss elements with experimentally determined material characteristics given in Tables 1 and 2. For shear reinforcement, three CFRP yarns were bundled in one truss element to reduce total computational time, while CFRP bars were modelled individually. The reinforcement was embedded in 8 node brick elements forming the concrete body with perfect bond. All parameters for concrete damaged plasticity model (CDPM) are listed in Figure 7 (right). Uniaxial compression behavior is predicted with the model by Sargin [68], and for simulation of concrete under tension, the model by Hillerborg [69] is

used. Calculation was performed with general/static increments of pressure on the loaded surface, with maximum step size 0.01 and minimum step size $1 \cdot 10^{-9}$, which represent a percentage of the maximum applied pressure.
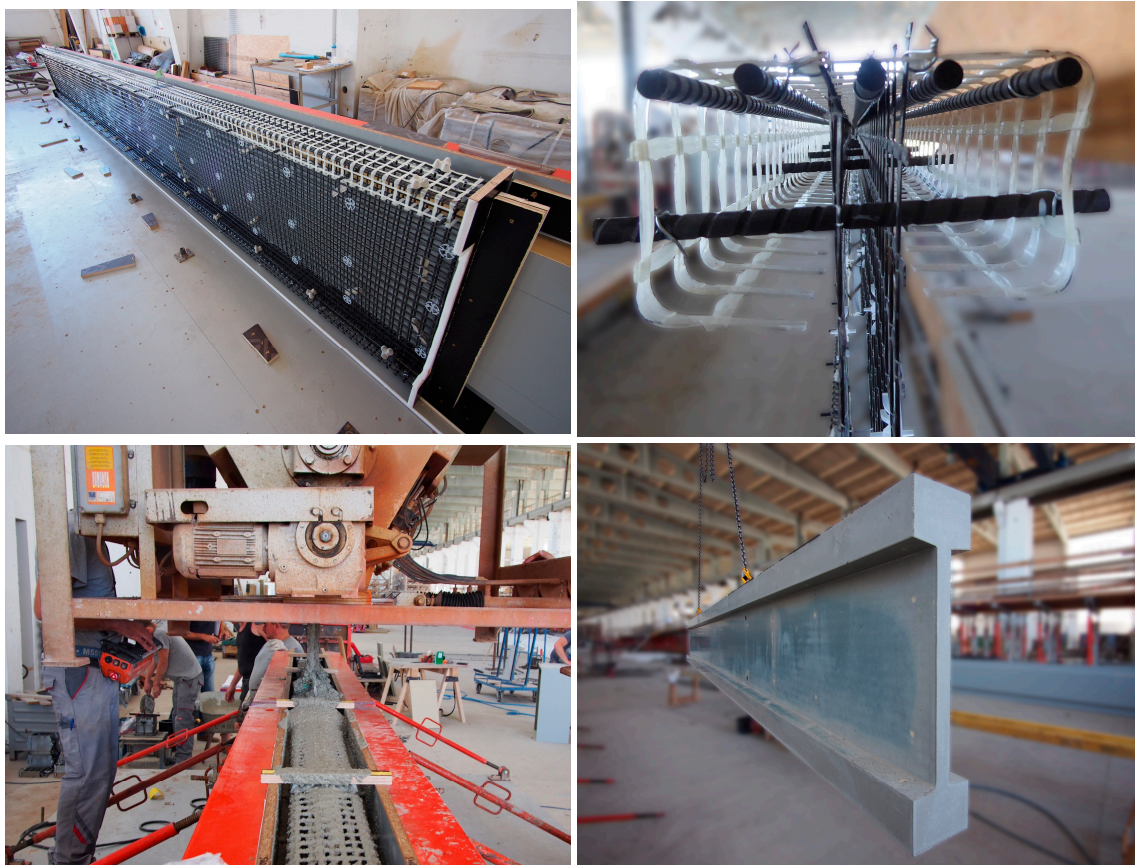
Figure 6. Production of I-beams in precast plant of Hentschke Bau GmbH: **top**: reinforcement cage and detail of FT01; **bottom**: casting and beam after demolding.
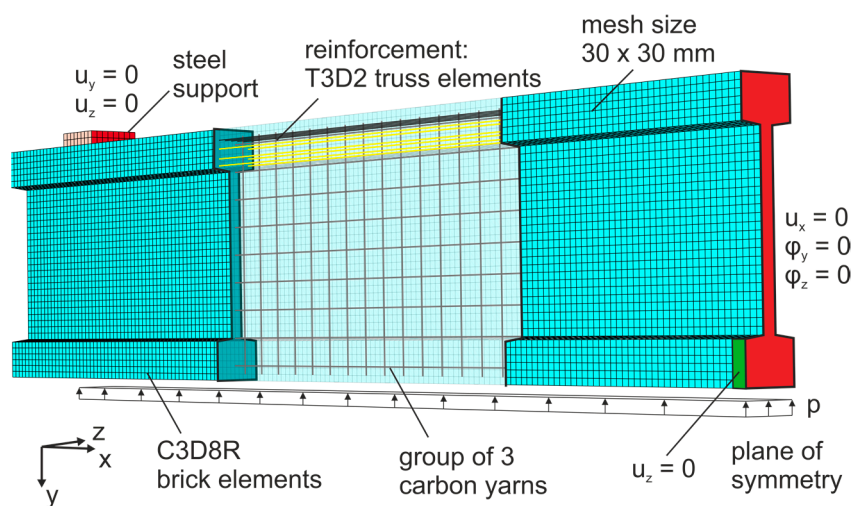

Figure 7. Schematic of input parameters and FE-mesh for FT01 simulation in *ABAQUS*. CDPM variables: $\psi = 50°$ [70]; $\varepsilon = 0.1$ [71]; $\sigma_{b0}/\sigma_{c0} = 1.16$ [71,72]; $K_c = 2/3$ [71,72]; $\mu = 0.0001$ [70]. Concrete: $D = 0.2$; $G_f = 73\, f_{cm}^{0,18}$ [17].

4. Results

4.1. Failure Mechanisms

As all beams were tested to failure, their distinctive fracture pattern gives insight on load-bearing mechanisms. With FT01, a brittle rupture of the main bending reinforcement in mid-span was observed at a total load of 686 kN (Figure 8). This was the predicted and desired failure mode. The sudden release of energy upon rupture of CFRP bars led to a brittle failure without residual load-bearing capacity. As secondary effect, the horizontal yarns of shear reinforcement ruptured and subsequently web concrete cover was spalled. No premature spalling of concrete in the tension chord or rupture of the glass grid could be observed prior to reaching ultimate load.

(**a**) (**b**)
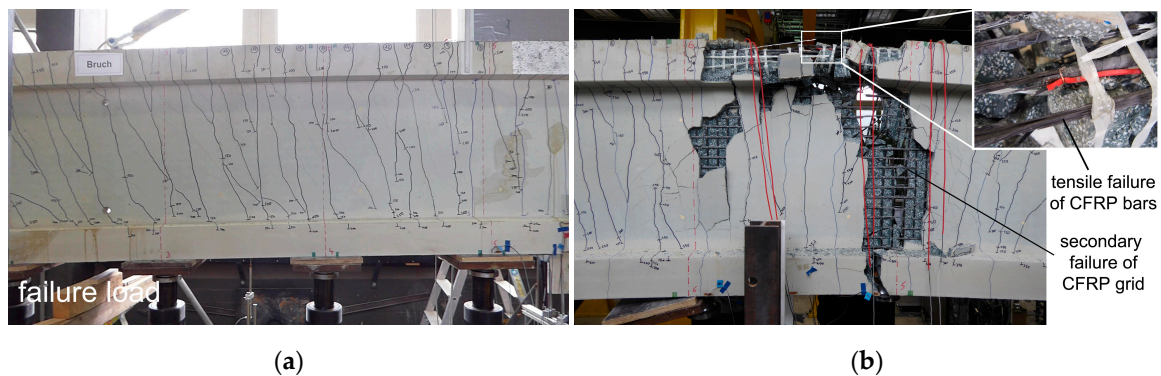
Figure 8. Failure of FT01: (**a**) beam at peak load 0.24 s prior to failure; (**b**) ruptured CFRP bars and secondary rupture of grid reinforcement with spalling of concrete.

FT02 was designed to fail in bending through failure of the compressive chord at approximately 1530 kN total load. Yet, at 1468.5 kN total load in the experiment (96% of the predicted load) a large part of the concrete cover in the last compression field near the support was split off and spalled. Subsequently, the shear zone failed in compression. All 20 bars of the longitudinal reinforcement and all four layers of textile grid were sheared-off in the angle of the shear crack (Figure 9). A sudden release of energy led to a brittle failure of the beam.

As FT03 was designed to evaluate the failure mechanisms of a full splice, the beam failed in mid-span at 52.7% of FT01's ultimate load, with longitudinal splitting cracks in the plane of the textile grid and perpendicular to the concrete surface, originating from one end of the splice (Figure 10). After side and top concrete cover were split off explosively, the splice was no longer able to carry loads. Transverse glass yarns were intact, while longitudinal yarns ruptured.
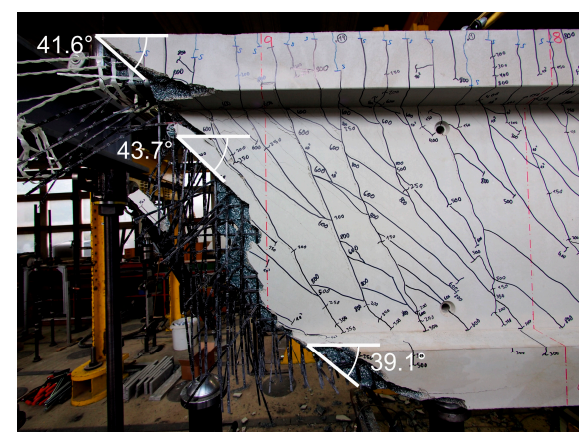
Figure 9. Failure of shear strut in compression near the support of FT02.

Figure 10. Failure sequence of FT03 in the overlap section in mid-span (Δt = 0.32 s).

4.2. Crack Pattern

All beams showed a dense crack pattern (Figure 11). As FT01 and FT02 had shrinkage cracks, first bending cracks opened from these existing cracks. FT03 had a first crack at 65 kN total load (56.9 kNm in mid-span). For all beams, first shear cracks formed out of bending cracks, with steeper angles near the center of the span and flatter angles towards the supports. At the range of failure load, new diagonal cracks with flatter angles formed in FT02 (Figure 12), crossing the existing bending-shear cracks.

4.3. Load-Deflection Behavior and Numerical Calculation

Beam FT01 and FT03 reveal a similar load-deflection behavior up to failure of FT03 (Figure 13, left). Numerical calculations with ABAQUS over-estimates cracking load. Ultimate load (−8%) and deflection of FT01 are well predicted. DamageT parameter for FT01 given in Figure 14 (top) shows damage similar to the observed crack pattern (Figure 11). Obviously, the real crack spacing cannot be predicted by this model, as bond-slip relation is not considered, shear reinforcement is bundled in groups of three yarns and mesh size is of the same magnitude as yarn spacing. The horizontal damage zone near the support of specimen FT02 is not a numerical error: A horizontal crack at the left end of the specimen actually occurred.

Numerical calculation of deflection for FT02 is comparable to the experimentally observed up to 75 mm deflection. Figure 14 (center) shows the DamageT and principal compressive strain trajectories at 850 kN total load where experimental and numerical curves are still congruent. Then, redistribution occurs, and a loss of stiffness caused by the shear zone combined with large shear distortions of elements results in increase of the calculated deflection. The DamageT plot for FT02 at 1450 kN (Figure 14, bottom) indicates the critical zone where failure occurred. This is in accordance with the observed failure in the compression field near the support. However, the model cannot predict the longitudinal cracking in the plane of the shear reinforcement with subsequent spalling of concrete cover, causing a brittle failure. This explains the overestimation of deformation in the simulation.
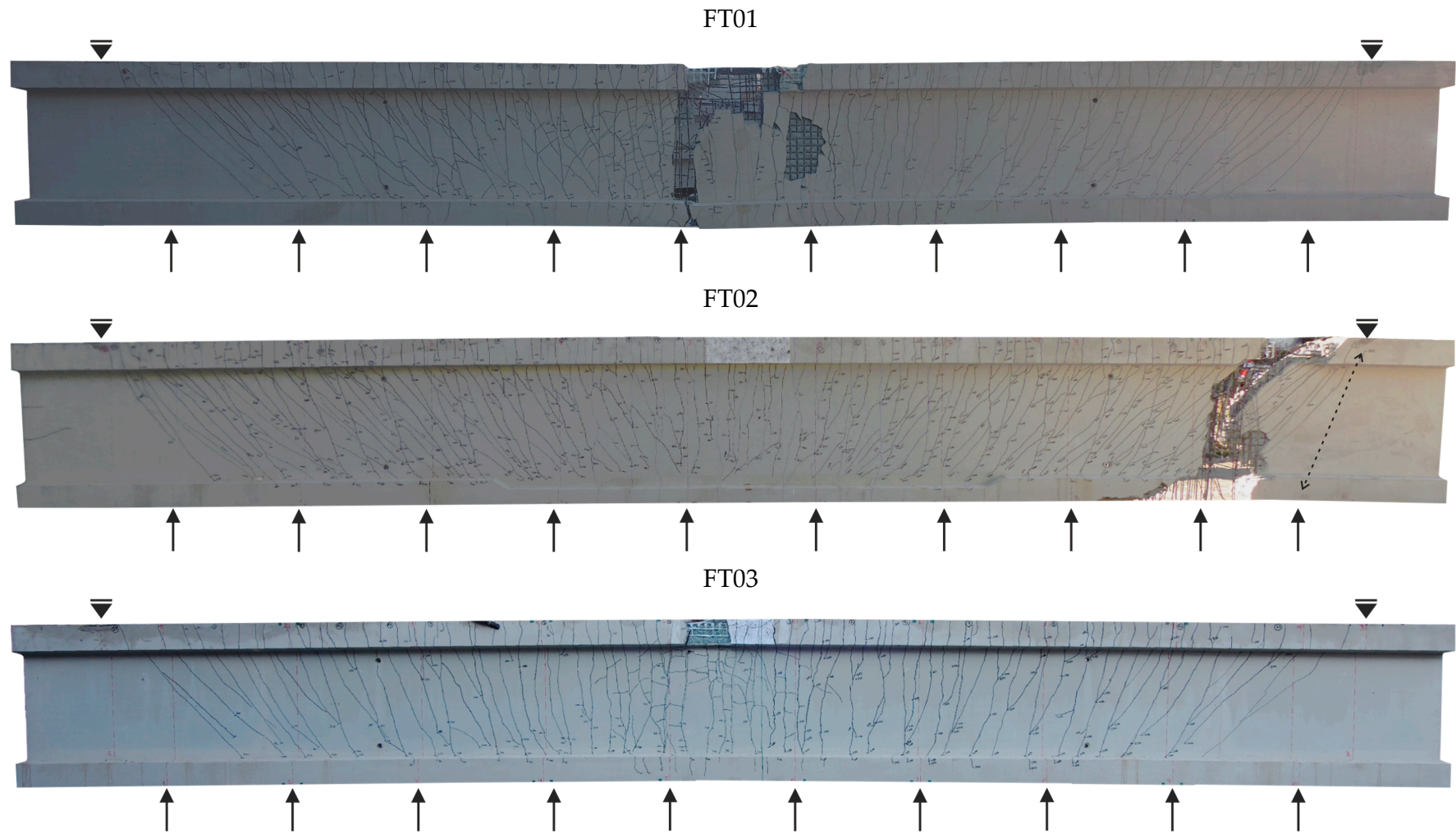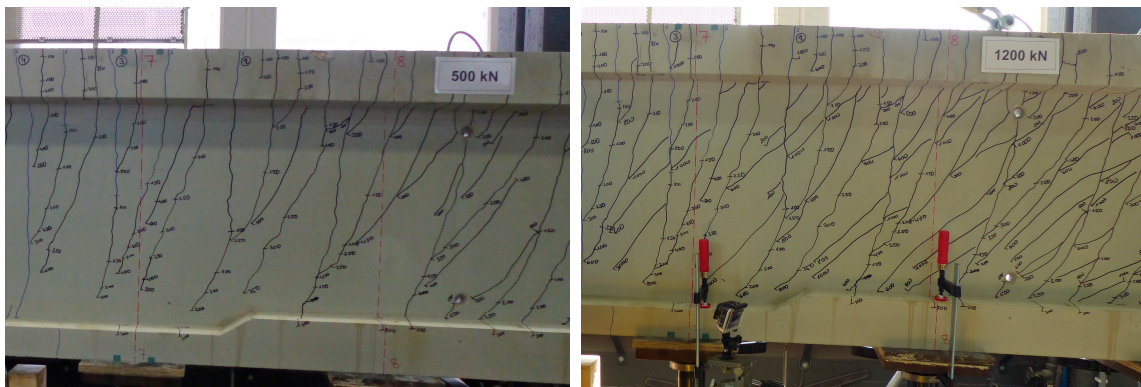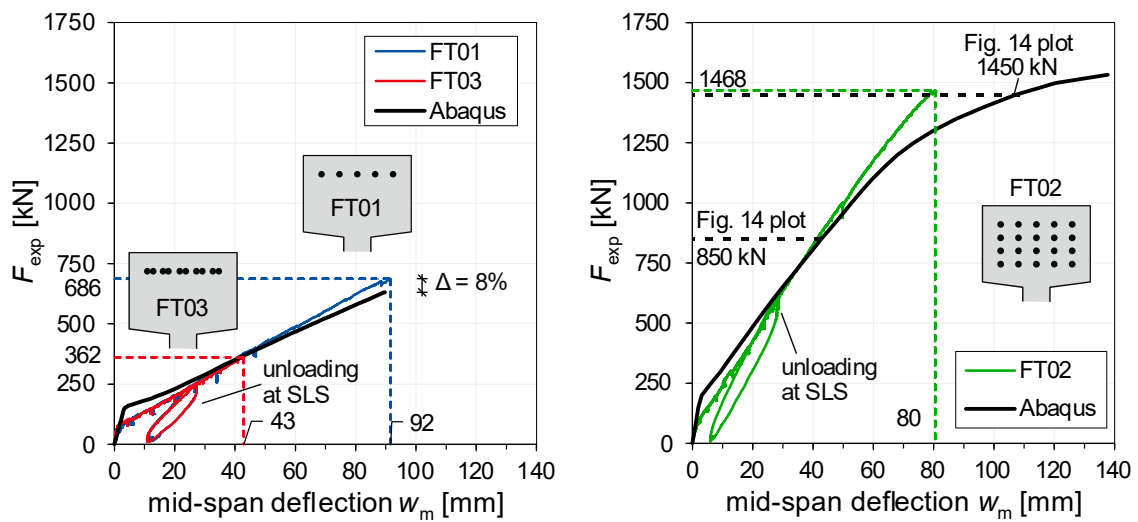
FT01

FT02

FT03

Figure 11. Crack pattern of beams FT01–FT03 after failure.

Figure 12. Change of inclination of bending-shear cracks at 500 kN and 1200 kN total load of specimen FT02.

Figure 13. Load-deflection-behavior of I-beams and results of numerical calculation.
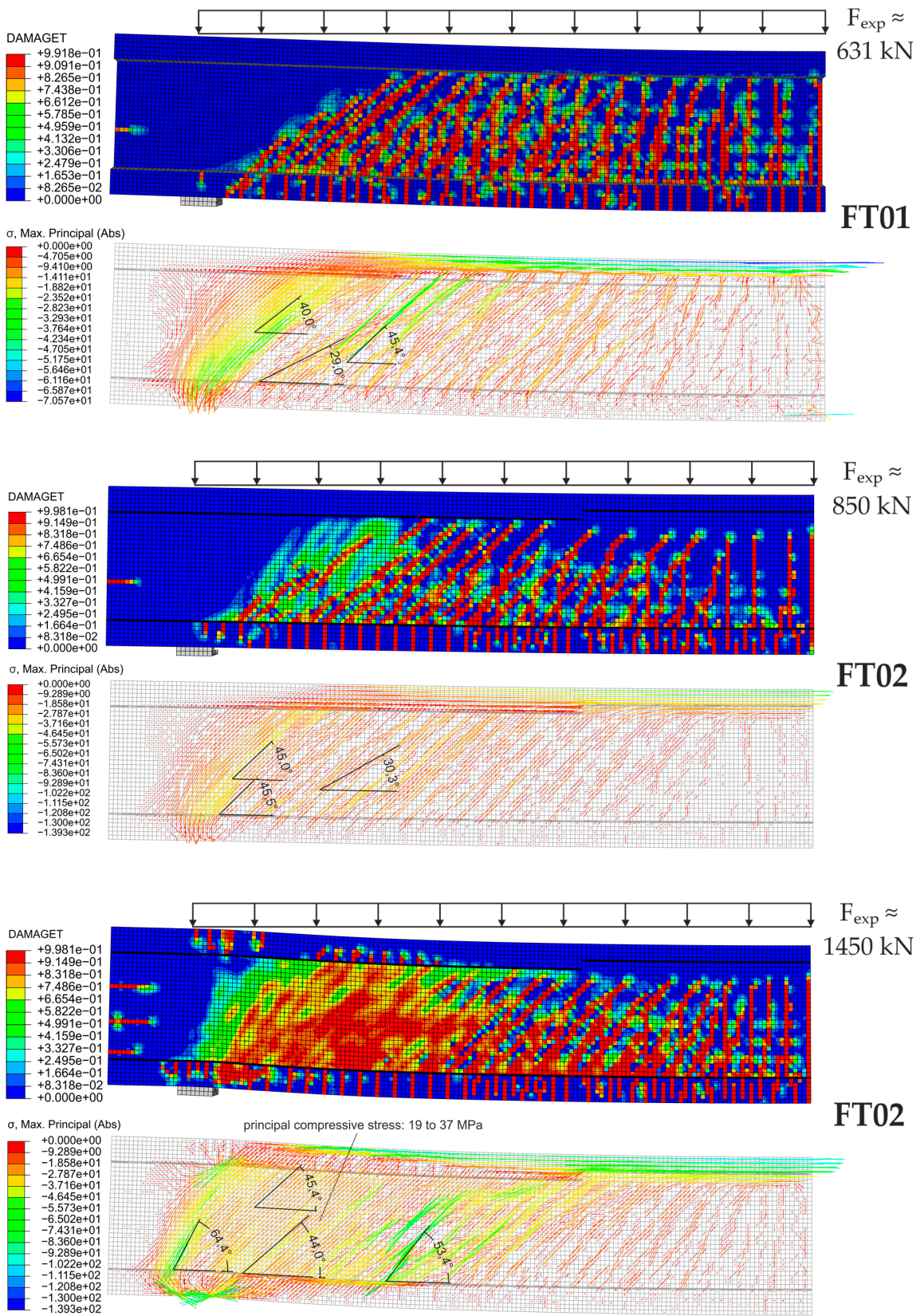
Figure 14. Results from FE-calculation: DamageT and principal compressive stress trajectories for FT01 and FT02.

5. Discussion

5.1. Prediction of Ultimate Strength

Prediction and verification of ultimate load is an essential step in design of reinforced concrete beams. Both methods, the manual calculation with spreadsheet using variations of linear strain distribution and non-linear FE analysis predict the ultimate load (and moment) in good accordance with the tests (Table 5). Although FT02 failed in shear, bending-compression failure was imminent, as can be concluded from measured strains of 2.66‰ in the compression zone at mid-span which were close to concrete failure strain of 2.67‰ measured in cylinder tests (Figure 15, bottom right). This explains the good agreement with predicted ultimate bending failure load.

With results from strain measurements on carbon bars in the outermost layer, a comparison with the assumed strain is possible. However, it should be noted that depending on the distance to the next bending crack and the effective length of debonding, the measured strain might be slightly reduced compared to the theoretical value. Linear increase of strain in the carbon bars indicates that the internal measurement was successful. Towards the end of the test FT01, strain gauges D2S, D4S, D5S and D3S failed. Concrete strain gauges D10C and D11C in FT02 (Figure 15, bottom right) show that the compression zone reached into the web of the beam, which is in accordance with calculations.

Table 5. Comparison of ultimate loads and strains in compression chord and main reinforcement.

		Experiment		Spreadsheet		ABAQUS	
	$M_{u,exp}$	F_{exp}	Strain	F_{calc}	Strain	F_{calc}	Strain
No.	**[kNm]**	**[kN]**	**[‰]**	**[kN]**	**[‰]**	**[kN]**	**[‰]**
FT01	600.23	686.0	$\varepsilon_{FRP} = 8.96$ * $\varepsilon_c = 1.73$ †	696.9	$\varepsilon_{FRP} = 11.04$ $\varepsilon_c = 1.71$	631.3	$\varepsilon_{FRP} = 10.73$ $\varepsilon_c = 1.81$
FT02	1284.93	1468.5	$\varepsilon_{FRP} = 6.74$ * $\varepsilon_c = 2.66$†	1534.2	$\varepsilon_{FRP} = 7.89$ $\varepsilon_c = 2.67$	1533.0	$\varepsilon_{FRP} = 9.06$ at 1450 kN: $\varepsilon_c = 3.18$
FT03	316.6	361.8	$\varepsilon_{FRP} = 5.81$ * $\varepsilon_c = 0.92$ †	-	-	-	-

* only strain gauges considered which were functional at ultimate load. † strain gauge D9C.

### 5.2. Failure of Compression Strut

The design of beam FT02 indicated that compression failure of the web might be governing at $\cot(\theta) = 1$ with a compressive stress resistance of $v_{Rm,max} = 0.6 \cdot (1 - 100/250) \cdot 100 = 36$ MPa. At failure, crack angles between 39.1° ($\cot(\theta) = 1.23$) and 43.7° ($\cot(\theta) = 1.05$) were observed (Figure 9, right). The results of FE calculations in Figure 14 (bottom) show that in the last compressive field near the support the principal compressive stress trajectories are inclined with 44° to 45.4° ($\cot(\theta) \approx 1$) at the level of experimental peak load. Compressive stresses in this region range from 19 to 37 MPa. This corresponds well with the assumptions in design. At lower load levels and towards mid-span, the angle of the compressive field is smaller, with 30.3° ($\cot(\theta) = 1.71$) (Figure 14 (center)). The model shows a redistribution of different compressive struts and the change of crack inclination throughout the test, which was also observed in the experiments (Figure 12).

With experimentally determined maximum shear force and the angle of compressive field from FE-results, reverse calculation of compressive stresses in the concrete struts at failure ($\sigma_{c,strut} = v_1 \cdot f_{cm}$) is possible (shown in (1)). As marked in Figure 11, the load from one of the five hydraulic cylinders acted within distance d from the support and was transferred directly to the support. Thus, it was not considered for ultimate shear load in the section of compressive failure of the web.

$$V_{Rm,max} = \frac{b_w \cdot z \cdot \sigma_{c,strut}}{(\cot\theta + \tan\theta)} \Rightarrow \frac{4}{10} \cdot 1.469\,MN = \frac{0.05 \cdot 0.9 \cdot 0.832 \cdot v_1 \cdot 100}{(1 + 1/1)} \Longleftrightarrow v_1 = 0.31 \qquad (1)$$

with: $z = 0.9 \cdot d = 0.9 \cdot 0.832$ m measured at the centroid of all 20 carbon bars in the shear crack after failure.

The strength reduction factor $\nu_1 = 0.6 \cdot (1 - f_c/250) = 0.36$ chosen in design is larger than the experimentally determined $\nu_1 = 0.31$. This additional reduction of concrete strength might be attributed to the dense reinforcement in the web. The artificial discontinuities of the yarns with lower transverse modulus of elasticity compared to concrete lead to out-of-plane stresses due to internal deviation of stress trajectories. Compressive tests on cubic specimen ($a = 50$ mm) with a similar concrete and the same reinforcement layout as a representative section of the web showed a reduction of ultimate strength of 10% with a restraint of transverse strain by the stiff loading plates of the testing equipment. Bochmann et al. observed similar strength reductions for textile-reinforced cubes in a constraint-free test setup where the compressive stress field is parallel to the reinforcement layers [73–75]. In both test campaigns, longitudinal cracking in the layer of the reinforcement led to failure in compression. The very same mechanism was observed at ultimate load of FT02, where longitudinal cracking in the layer of shear reinforcement in the web and subsequent spalling of the concrete cover initiated failure of the compressive strut.
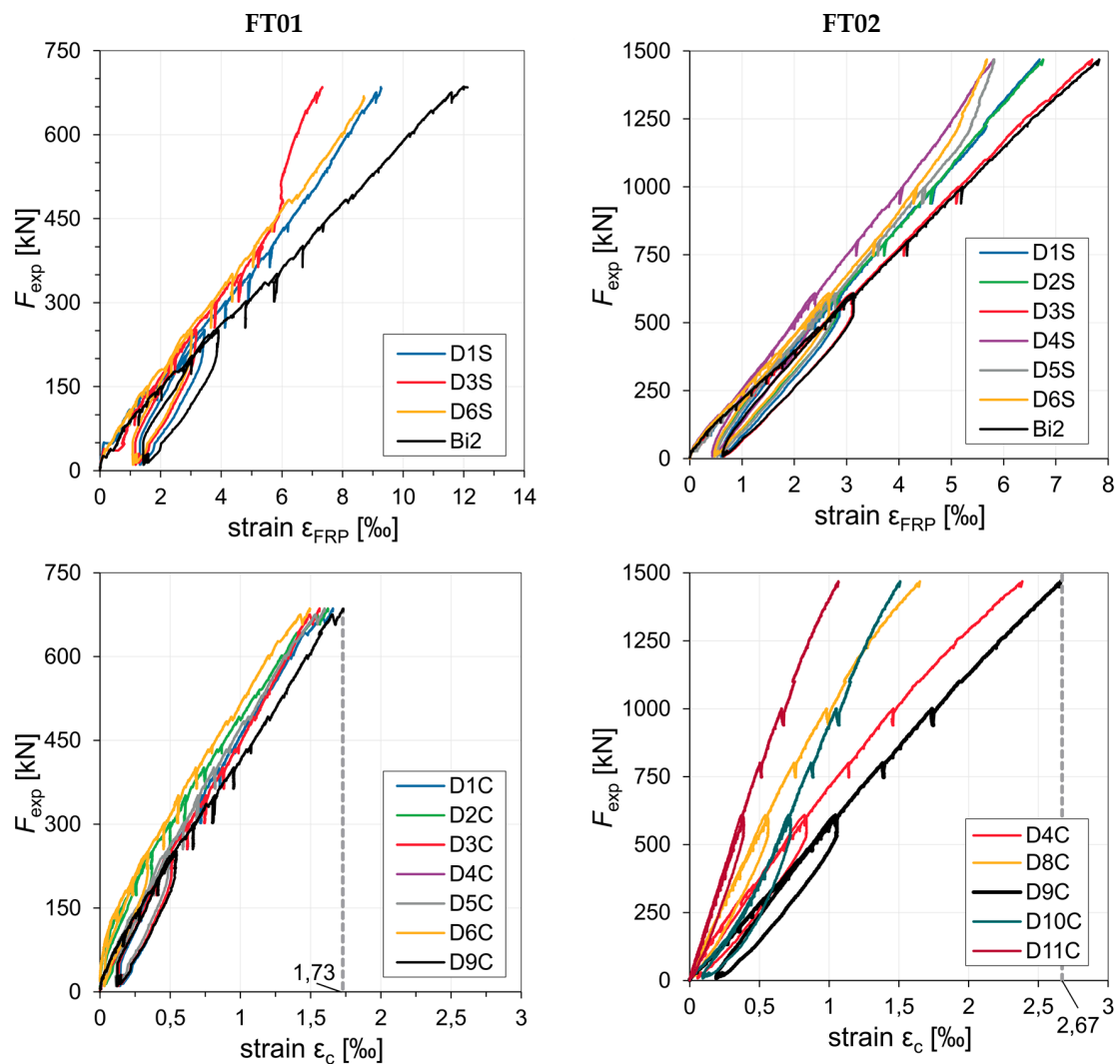
Figure 15. Strain measurements for FT01 (**left**) and FT02 (**right**) indicating that good prediction of strain distribution with spreadsheet calculation is possible.

In addition to the effect of local discontinuities, the concrete is subjected to out-of-plane stress through bond of textile reinforcement (splitting stress). This combined in-plane/out of plane stress has not been investigated in compressive tests on textile reinforced specimens, yet.

It can be concluded that existing pure truss models for verification of compressive struts neglecting aggregate interlock, dowel action of longitudinal reinforcement and a shear contribution of the compressive zone might be transferred to textile-reinforced shear zones when strength reduction factor v_1 is modified to account for dense textile reinforcement parallel to the compressive field. Future tests specifically designed for shear compression failure in realistic scale as well as small-scale tests on combined compression/out of plane tension are necessary to deepen the knowledge of the necessary reduction factor.

5.3. Lap Length

The lap length of 500 mm in FT03 failed prematurely by splitting of the concrete cover and was not able to provide the capacity necessary to reach the same ultimate load as FT01. Assuming the same bond conditions as in pull-out material tests (Table 2), an anchorage length of 115 mm would have been sufficient for one individual bar. However, this assumption neglects failure mechanisms of concrete splitting in a lap of five carbon bars, which does not occur in pull-out tests. Using mean bond strength from from Eurocode 2 [63,64], clause 8.4.2, with concrete characteristics from Table 4, the lap length increased with the coefficient for multiple bars spliced in one section (α_6) results in:

$$l_0 = \alpha_6 \cdot \frac{\varnothing}{4} \cdot \frac{\sigma_{nm}}{2.25 \cdot f_{ctm}} = 1.4 \cdot \frac{8.85}{4} \cdot \frac{1828}{2.25 \cdot 4.77} = 528 \; mm \tag{2}$$

Although this value is slightly larger than the given 500 mm, it does not explain a decrease to 53% of FT01's ultimate bending capacity. Figure 10 clearly shows that the loss of bond of the CFRP bars leading to failure of the beam was caused by splitting of the concrete cover. After a pronounced pattern of bending cracks, horizontal splitting cracks in the plane of the preformed stirrups occurred, spalling off the complete concrete cover of the tension chord. Then the preformed reinforcement cage of the stirrups opened, and the confinement action of the transverse reinforcement was lost. The horizontal stress from the planar splice could no longer be restrained, even if the glass yarns in transverse direction were still intact. From the crack development can be assumed that a larger concrete cover would not have increased resistance to longitudinal cracking of concrete in the plane of the preformed glass grid. A significant portion of the concrete in this plane is disturbed by the presence of textile and could not contribute to tensile resistance perpendicular to it. A larger spacing in longitudinal and transverse direction might increase resistance to longitudinal cracking, but meanwhile the cross-sectional area of yarns would need to be increased to maintain the same amount of reinforcement area. An alternative explanation for the premature lap failure could be the very high bond capacity of the carbon bars, which caused localized cracking at the outset of the splice with extensive horizontal cracking. The failure starts at one side of the splice (see Figure 10), and cracks run from left to right (zipper effect). The few glass yarns provided by the pre-formed stirrup grid with relatively low stiffness were unable to confine the lap length effectively.

5.4. Compatibility of FRP Rebar and Grids

Combinations of reinforcements with different material characteristics for strength, modulus of elasticity and bond are well-known from steel-reinforced concrete: Bonded prestressing strands and mild steel rebar differ substantially regarding ultimate strength, strain, and bond properties, while their modulus of elasticity is very similar. In principle, the relationships derived for steel reinforced concrete are transferable to mixed FRP reinforced sections, because FRP grids and FRP bars are of the same type (bundles of uniaxial continuous fibers with anisotropic behavior) and are subject to the same load-bearing principles. Yet, those reinforcements differ in one essential point from steel: Their lack of yield capacity and their brittle failure. In consequence, different bond and stiffness

need to be considered not only in SLS (as it is usual for mixed steel reinforced sections) but also in ULS. For the beams described in this paper, this was taken into account by choosing glass grids as stirrups in the tension chords. Their lower modulus of elasticity allows higher strains in longitudinal direction parallel to the main CFRP reinforcement at rupture, and thus premature failure with spalling of the concrete was prevented. By assuming perfect bond in cross-sectional verification for bending, differences in bond strength were not considered. Pre-formed textile grids with their mechanical interlock exhibit high bond stresses, potentially better strengths than CFRP bars, depending on their surface treatment. A redistribution of tensile stresses in bending cracks towards the better bonded component can be assumed. With given bond–slip-relations for reinforcement materials, the numerical solution of the differential equation system for bond can be used to calculate the stress distribution along the embedment length. While this procedure is suitable for research, simpler detailing rules for practical applications are to be developed.

The definition of cross-sectional area for FRP rebar (nominal, core diameter) and textile grids (effective, filament area) differs. In principle, the definition is arbitrary if the same reference value is used for stress and stiffness. This is true for cross-sectional verification of bending. However, if geometrical properties are derived from cross-sectional areas, this is disputable. For example shear verification in Eurocode 2 [64] for structural elements without shear reinforcement uses geometrical reinforcement ratio, which implicitly accounts for dowel action. It is known that resistance of dowels depends on cross-sectional stiffness of the individual reinforcement element. Also, for detailing specifications (maximum/minimum reinforcement ratios), a general definition of cross-sectional area for mixed reinforcement would be recommended.

The large-scale tests show that compatibility of impregnated textiles and CFRP bars is given. While CFRP bars contribute large cross-sectional areas and thus high bending tensile resistance, the distributed textile shear reinforcement bridges shear cracks efficiently. Short anchorage length in compression and tension chords for the straight yarns are advantageous, while good bond and the multitude of yarns produce a dense shear crack pattern. Yet, enabling the intersection of the dense planar shear reinforcement and preformed stirrup reinforcement is challenging. With matched yarn spacing of high-quality reinforcement, which is dimensionally accurate, it becomes possible for small and medium-sized elements.

5.5. Prediction of Deflection

At serviceability limit state (SLS), a deformation at midspan of $w = L/250 = 28$ mm is permitted, corresponding to the limit defined in [64]. To compare the quality of the calculation approaches, the moment applied in the test at a deflection of 28 mm is used as input value for the deflection calculation. A manual calculation with the method by Branson [76], a piecewise integration based on the moment-curvature diagram and a non-linear FE-calculation with *ABAQUS* were performed.

In Equation (3), the adaption of the original Branson equation by Bischoff and Scanlon [77–79] for calculation of the effective moment of inertia I_e is given:

$$I_e = \frac{I_{cr}}{1 - \gamma\left(\frac{M_{cr}}{M_a}\right)^2\left[1 - \frac{I_{cr}}{I_g}\right]} \leq I_g \quad for \quad M_a \geq M_{cr} \tag{3}$$

with:

$\gamma = 1.72 - 0.72\left(\frac{M_{cr}}{M_a}\right)$, Factor for structural system with continuous loads according to [78,79]
I_{cr} *and* I_g, moment of inertia of cracked and uncracked section
M_{cr} *and* M_a, moment at first cracking and moment at SLS

The moment of inertia of the cracked section, I_{cr}, was calculated considering all longitudinal reinforcement layers including longitudinal yarns from shear reinforcement with their respective lever arm. Using I_e, deflection in mid span is calculated with equations from linear-elastic structural

analysis. The moment at first cracking has a large influence on calculation results. Thus, the accuracy of the results depends to a large extent on concrete tensile strength. Eigen stresses (e.g., resulting from drying shrinkage) need to be considered, as they reduce the first cracking moment. Table 6 shows the influence of M_{cr} on predicting deflection. Using tensile strength $f_{ct} = 1.0 \cdot f_{ct,sp}$ as given in Table 4 and the section modulus W_y of the uncracked cross-section, the theoretical moment at first cracking is 111.3 kNm. Bischoff and Gross [79] propose a reduction to 80% to account for eigen stresses. As FT01 was pre-cracked, no experimental first cracking moment could be determined. Employing uncracked specimen FT03, the ratio of experimental to theoretical first cracking moment results in 57.6%. Applying this reduction to calculation for FT01 and FT02 gives the best results. The prediction for higher reinforced FT02 with its smaller ratio of M_a/M_{cr} is less affected by changes of M_{cr}, which is in accordance to statements in [80].

Results of the second calculation method by piecewise numerical integration with Simpson's rule based on moment-curvature (M-κ) relation are given in Table 6 (center). The theoretical M-κ curve (Figure 16) is derived using material characteristics and geometrical properties of cracked and uncracked section. The four points defining the yellow curve in Figure 16 ($x = \kappa$, $y = M$) are P0 [0|0], P1 [0.576% $\cdot$ M_{cr} / ($E_{cm} \cdot I_g$) | 0.576% $\cdot$ M_{cr}], P2 [1.3 $\cdot$ 0.576% $\cdot$ M_{cr} / ($E_{cm} \cdot I_{cr}$) | (1.3 $\cdot$ 0.576% $\cdot$ M_{cr})] and P3 [$M_{u,cal}$ / ($E_{cm} \cdot I_{cr}$) | $M_{u,cal}$]. M-κ experimental is taken from strain gauge measurements at the compression chord and strains in the tension flange determined by LVDT (D9C and Bi2 in Figure 3). Both calculations yield good predictions of the obtained experimental values. Taking into account shear strains would further improve prediction of deflection quality. However, the results also rely on a realistic estimate of first cracking moment.

Table 6. Prediction of deflection with Equation (3), with M-κ-relation and with FE-model.

| No. | M_{exp} | w_{exp} | I_{cr} | Branson/Bischoff | | | | M-κ theor. | M-κ exp. | ABAQUS |
				M_{cr}	γ	I_e	w_{calc}	w_{calc}	w_{calc}	w_{calc}
	[kNm]	[mm]	[cm^4]	[kNm]	[-]	[cm^4]	[mm]	[mm]	[mm]	[mm]
FT01	229.7	28	106,334	115.5 (100%)	1.35	152,248	19.9 (−28.9%) *	28.2 (+0.7%) *	25.7 (−8.2%) *	25.6 (−8.6%) *
				92.4 (80%)	1.42	133,463	22.7 (−18.9%) *			
				66.6 (57.6%)	1.50	119,666	25.3 (−9.6%) *			
FT02	515.7	28	275,512	105.4 (100%)	1.56	288,145	22.9 (−18.2%) *	23.9 (−14.6%) *	23.3 (−16.7%) *	26.1 (−6.6%) *
				84.3 (80%)	1.59	283,616	23.3 (−16.8%) *			
				60.7 (57.6%)	1.63	279,742	23.6 (−15.7%) *			

* deviation to the experimental deflection of 28 mm.

Finally, non-linear FE-analysis was employed to predict the deflection of SLS (Table 6, right column). Quality of all results depends mainly on material input values. Over-estimation of first cracking load for FT01 and FT02 can be explained with eigen stress from dry shrinkage and shrinkage cracks.

For prediction of deflection in practice, all three methods seem suitable. Especially the easy-to-use hand calculations based on simple mechanical relations allow for quick and realistic estimates of deflection, if the reduction of tensile strength by eigen stress is considered. However, for verification of long-term deflections, a reduced modulus of elasticity for concrete should be considered accounting for creep strain.

5.6. Utilization Ratio of Carbon Bars–SLS to ULS Reserve

CFRP reinforcement is costly, and thus a high utilization ratio of material strength is a major goal. High utilization means that reinforcement necessary for satisfying SLS deflection limits is utilized in ULS up to design strength. This discussion is known from high-strength steel in conventional reinforced concrete, which is usually utilized in flexural members only for prestressing.
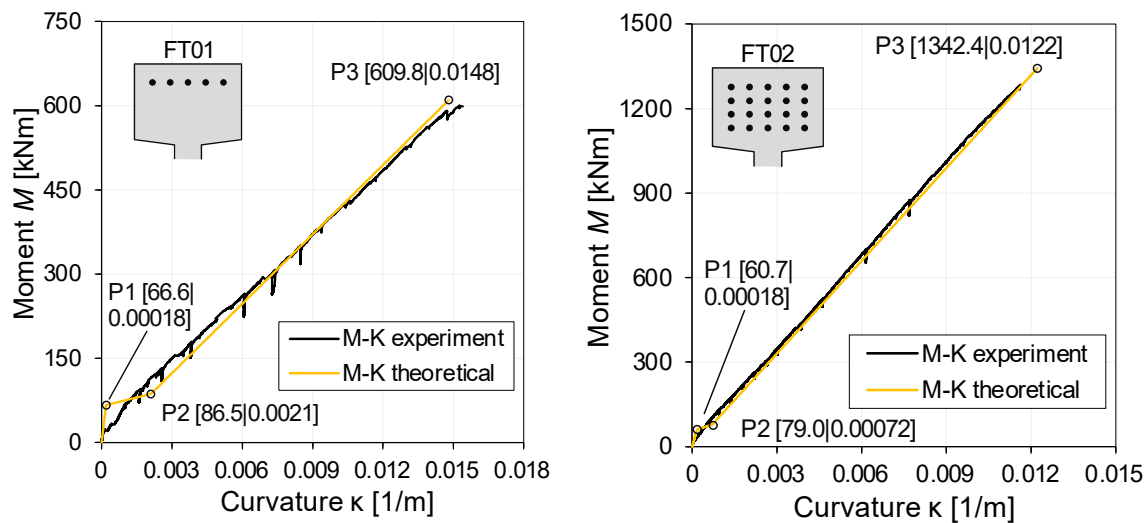
Figure 16. Theoretical and experimentally obtained *M*-κ curve for FT01 (**left**) and FT02 (**right**).

Based on strain gauge measurements in specimen FT01, the main CFRP bar reinforcement in SLS (at 28 mm short-term deflection) was utilized at 542 MPa, 30% of mean CFRP material strength. In design, the strength reserve of 70% is required for incorporation of time-dependent material strength reduction coefficients and material and load safety factors (SLS to ULS reserve).

In specimen FT02 which was designed for flexural compression failure, strain measurements show that the reinforcement was subjected to at a lower stress of 450 MPa (25% of material strength). As the outermost reinforcement at ULS was strained only up to 6.74‰ (1115 MPa), overall utilization ratio of reinforcement for FT02 is lower than for FT01. This ratio would further decrease if deflection in SLS increases through creep of concrete. The comparison of the reinforcement layout of both beams indicates that design for flexural compression failure while maintaining deflection limits is cost-intensive with non-prestressed reinforcement. The obvious solution for this case would be to apply low-level prestressing, staggered over the height of the beam to arrive at the same strain in ULS in all layers. Thus, strain reserves are preserved to account for necessary increase of reinforcement strain between SLS and ULS loading (see also recommendations in [81]). Meanwhile, eccentric pretensioning increases precamber and thus reduces sag in SLS.

The discussion which failure mode is more ductile, flexural tension or flexural compression failure, and thus favourable for design of CFRP reinforced structures is ongoing and not pursued in detail here. The authors are convinced that maintaining a sufficient strain and deflection reserve combined with pronounced cracking during load increase between SLS and ULS (as seen for the beams in this study) might serve as adequate announcement of failure. This can be interpreted as a ductile structural behaviour despite the brittleness of failure of CFRP and high-strength concrete in material tests. It could be an acceptable substitute for yielding of main steel reinforcement, which may lead to a similar deflection, large crack widths and eventually a ductile post-peak load behaviour for conventional reinforced beams with flexural failure. In this context, high-level prestressing of principal CFRP reinforcement for beams is not recommended, as it prevents pronounced cracking prior to failure of main reinforcement.

6. Conclusions

In this study, three large-scale I-beams with mixed CFRP and textile reinforcement were tested to failure. Evaluation of results, accompanying numerical analysis and theoretical discussion led to the following conclusions:

- Production of beams with CFRP and textile reinforcement is feasible with methods available in precast production plants.
- Impregnated textile CFRP grids are well suited as shear reinforcement for I-beams with large effective depth, creating a dense crack pattern and bridging shear cracks efficiently. Through their short anchorage length, straight yarn ends were suitable to anchor shear reinforcement in tension and compression chord.
- Compatibility of CFRP bars and CFRP textiles is given when strain limits of different reinforcement types are considered in design. Premature rupture and premature spalling of concrete needs to be prevented.
- Calculation of ultimate load at bending failure with variation of linear strain distribution and with geometrical and physical non-linear FE-calculation delivers accurate results.
- Prediction of deflection with existing hand-calculation methods derived for steel- or FRP reinforced concrete is feasible if realistic tensile strength is assumed, accounting for eigen stress caused e.g., by concrete shrinkage. FE-calculations are suitable for SLS, as well.
- Shear failure of compressive struts of specimen FT02 can be explained through further reduction of compressive strength by dense textile reinforcement in the web compared to the reduction factor ν_1 from [64] assumed in design.
- Beam FT03 with 500 mm planar splice of the main reinforcement in mid-span failed prematurely at about 53% of the identical beam FT01 without splice. Splitting of concrete cover in the plane of pre-formed stirrup reinforcement was identified as failure mechanism. Pre-formed open glass FRP grids were inadequate for an effective lateral confinement of the splice.

Future research should focus on detailing specifications for mixed CFRP bar/textile reinforcement. Studies on staggered prestressing might increase utilization ratio of CFRP reinforcement. Shear design models accounting for contribution of distributed textile shear reinforcement and concrete are to be developed in the future. Additional experimental studies on beams with large effective depth dimensioned for shear failure are required for this purpose.

Conflicts of Interest: The authors declare no conflict of interest. The founding sponsors had no role in the design of the study; in the collection, analyses, or interpretation of data; in the writing of the manuscript, and in the decision to publish the results.

References

1. Bielak, J.; Hegger, J.; Chudoba, R. Towards Standardization: Testing and Design of Carbon Concrete Composites. In *High Tech Concrete: Where Technology and Engineering Meet, Proceedings of the 2017 FIB Symposium, Maastricht, The Netherlands, 12–14 June 2017*; Hordijk, D.A., Luković, M., Eds.; Springer International Publishing: Cham, Switzerland, 2017; pp. 313–320, ISBN 3319594710.

2. Hegger, J.; Curbach, M.; Stark, A.; Wilhelm, S.; Farwig, K. Innovative design concepts: Application of textile reinforced concrete to shell structures. *Struct. Concr.* **2018**, *19*, 637–646. [CrossRef]

3. Kromoser, B.; Preinstorfer, P.; Kollegger, J. Building lightweight structures with carbon-fiber-reinforced polymer-reinforced ultra-high-performance concrete: Research approach, construction materials, and conceptual design of three building components. *Struct. Concr.* **2019**, *20*, 730–744. [CrossRef]

4. May, S.; Michler, H.; Schladitz, F.; Curbach, M. Lightweight ceiling system made of carbon reinforced concrete. *Struct. Concr.* **2018**, *19*, 1862–1872. [CrossRef]

5. Scholzen, A.; Chudoba, R.; Hegger, J.; Will, N. Leichte Dachschalen aus Carbonbeton. *Beton- und Stahlbetonbau* **2016**, *111*, 663–675. [CrossRef]

6. Preinstorfer, P.; Kromoser, B.; Kollegger, J. Flexural behaviour of filigree slab elements made of carbon reinforced UHPC. *Constr. Build. Mater.* **2019**, *199*, 416–423. [CrossRef]

7. Kahnt, A.; Schladitz, F.; Tietze, M.; Scheerer, S.; Curbach, M. Carbonbeton—Hochleistungsbaustoff mit Effizienzpotenzial. *DETAIL* **2016**, *2016*, 302–308.

8. Spelter, A.; Bergmann, S.; Bielak, J.; Hegger, J. Long-Term Durability of Carbon-Reinforced Concrete: An Overview and Experimental Investigations. *Appl. Sci.* **2019**, *9*, 1651. [CrossRef]

9. Herbrand, M.; Adam, V.; Classen, M.; Kueres, D.; Hegger, J. Strengthening of Existing Bridge Structures for Shear and Bending with Carbon Textile-Reinforced Mortar. *Materials* **2017**, *10*, 1099. [CrossRef]

10. Scheerer, S.; Zobel, R.; Müller, E.; Senckpiel-Peters, T.; Schmidt, A.; Curbach, M. Flexural Strengthening of RC Structures with TRC—Experimental Observations, Design Approach and Application. *Appl. Sci.* **2019**, *9*, 1322. [CrossRef]

11. Grace, N.F.; Jensen, E.A.; Eamon, C.D.; Shi, X. Life-Cycle Cost Analysis of Carbon Fiber-Reinforced Polymer Reinforced Concrete Bridges. *ACI Struct. J.* **2012**, *109*, 697–704. [CrossRef]

12. Cadenazzi, T.; Dotelli, G.; Rossini, M.; Nolan, S.; Nanni, A. Life-Cycle Cost and Life-Cycle Assessment Analysis at the Design Stage of a Fiber-Reinforced Polymer-Reinforced Concrete Bridge in Florida. *Adv. Civ. Eng. Mater.* **2019**, *8*, 128–151. [CrossRef]

13. Rempel, S.; Kulas, C.; Will, N.; Bielak, J. Extremely Light and Slender Precast Pedestrian-Bridge Made Out of Textile-Reinforced Concrete (TRC). In *High Tech Concrete: Where Technology and Engineering Meet, Proceedings of the 2017 FIB Symposium, Maastricht, The Netherlands, 12–14 June 2017*; Hordijk, D.A., Luković, M., Eds.; Springer International Publishing: Cham, Switzerland, 2017; pp. 2530–2537. ISBN 3319594710.

14. Bielak, J.; Bergmann, S.; Hegger, J. Querkrafttragfähigkeit von Carbonbeton-Plattenbrücken mit C-förmiger Querkraftbewehrung. *Beton-und Stahlbetonbau* **2019**, *114*, 465–475. [CrossRef]

15. Schumann, A.; Michler, H.; Schladitz, F.; Curbach, M. Parking slabs made of carbon reinforced concrete. *Struct. Concr.* **2018**, *19*, 647–655. [CrossRef]

16. Otto, J.; Adam, R. Carbonbeton und Stahlbeton im wirtschaftlichen Vergleich. *Bauingenieur* **2019**, *94*, 246–252.

17. International Federation for Structural Concrete. *FIB Model Code for Concrete Structures 2010*; Ernst & Sohn: Berlin, Germany, 2013.

18. Canadian Standards Association. *Design and Construction of Building Structures with Fibre-Reinforced Polymers*; CSA S806-12:2012-03; Canadian Standards Association: Mississauga, ON, Canada, 2012.

19. American Concrete Institute. *Guide for the Design and Construction of Structural Concrete Reinforced with Fiber-Reinforced Polymer (FRP) Bars*; ACI 440.1R-15; American Concrete Institute: Farmington Hills, MI, USA, 2015.

20. Lieboldt, M.; Tietze, M.; Schladitz, F. C^3-Projekt—Erfolgreiche Partnerschaft für Innovation im Bauwesen. *Bauingenieur* **2018**, *93*, 265–273.

21. Hegger, J.; Kulas, C.; Horstmann, M. Realization of TRC façades with impregnated AR-glass textiles. *Key Eng. Mater.* **2011**, *466*, 121–130. [CrossRef]

22. Kulas, C.; Schneider, M.; Will, N.; Grebe, R. Hinterlüftete Vorhangfassaden aus Textilbeton. *Bautechnik* **2011**, *88*, 271–280. [CrossRef]

23. Hegger, J.; Kulas, C.; Raupach, M.; Büttner, T. Tragverhalten und Dauerhaftigkeit einer schlanken Textilbetonbrücke. *Beton-und Stahlbetonbau* **2011**, *106*, 72–80. [CrossRef]

24. Kueres, S.; Will, N.; Hegger, J. Flexural design of a modular footbridge system with pretensioned carbon fiber reinforced polymer reinforcement. *Struct. Concr.* **2019**, *20*, 1858–1870. [CrossRef]

25. solidian GmbH. *Allgemeine Bauaufsichtliche Zulassung: Kleingebäude, Raumzellen (Fertiggarage)*. Z-71.3-40. 2018. Available online: https://www.solidian.com/fileadmin/user_upload/pdf/solidian_Z-71.3-40_abZ_Garagen.pdf (accessed on 5 June 2020).

26. Kueres, S. Analysis and Design of Concrete Beams with Pre-Tensioned CFRP Reinforcement. Ph.D. Thesis, RWTH Aachen University, Aachen, Germany, 2019. [CrossRef]

27. Schumann, A.; May, S.; Curbach, M. Design and Testing of Various Ceiling Elements Made of Carbon Reinforced Concrete. *Proceedings* **2018**, *2*, 543. [CrossRef]

28. Chudoba, R.; Sharei, E.; Senckpiel-Peters, T.; Schladitz, F. Numerical modeling of non-uniformly reinforced carbon concrete lightweight ceiling elements. *Appl. Sci.* **2019**, *9*, 2348. [CrossRef]

29. Kulas, C. Zum Tragverhalten getränkter textiler Bewehrungselemente für Betonbauteile. Ph.D. Thesis, RWTH Aachen University, Aachen, Germany, 2013.

30. Kromoser, B.; Huber, P.; Preinstorfer, P. Experimental study of the shear behaviour of thin walled CFRP reinforced UHPC structures. In *Better, Smarter, Stronger, Proceedings of the 2018 FIB Congress, Melbourne, Australia, 7–11 October 2018*; Foster, S., Gilbert, I.R., Mendis, P., Al-Mahaidi, R., Millar, D., Eds.; Federation internationale du beton: Lausanne, Switzerland, 2018; pp. 1744–1750.

31. Bielak, J.; Hegger, J.; Schmidt, M. Shear Capacity of Carbon Fibre Textile Reinforced Concrete Slabs with Planar and C-Shaped Shear Reinforcement. In Proceedings of the Fiber Reinforced Polymer Reinforced Concrete Structures 14, Belfast, UK, 4–7 June 2019.

32. Bischoff, P.H. Comparison of Existing Approaches for Computing Deflection of Reinforced Concrete. *ACI Struct. J.* **2020**, *117*, 231–240. [CrossRef]

33. Chudoba, R.; Vořechovský, M.; Konrad, M. Stochastic modeling of multi-filament yarns: I. Random properties within the cross-section and size effect. *Int. J. Solids Struct.* **2006**, *43*, 413–434. [CrossRef]

34. Rempel, S. Zur Zuverlässigkeit der Bemessung von biegebeanspruchten Betonbauteilen mit textiler Bewehrung. Ph. D. Thesis, RWTH Aachen University, Aachen, Germany, 2018. [CrossRef]

35. Hinzen, M. Prüfmethode zur Ermittlung des Zugtragverhaltens von textiler Bewehrung für Beton. *Bauingenieur* **2017**, *92*, 289–291.

36. Vorechovský, M.; Chudoba, R. Stochastic modeling of multi-filament yarns: II. Random properties over the length and size effect. *Int. J. Solids Struct.* **2006**, *43*, 435–458. [CrossRef]

37. Vorechovsky, M.; Rypl, R.; Chudoba, R. Probabilistic crack bridge model reflecting random bond properties and elastic matrix deformation. *Compos. Part B: Eng.* **2018**, *139*, 130–145. [CrossRef]

38. Rempel, S.; Ricker, M. Ermittlung der Materialkennwerte der Bewehrung für die Bemessung von textilbewehrten Bauteilen. *Bauingenieur* **2017**, *92*, 280–288.

39. Bielak, J.; Spelter, A.; Will, N.; Claßen, M. Verankerungsverhalten textiler Bewehrungen in dünnen Betonbauteilen. *Beton- und Stahlbetonbau* **2018**, *113*, 515–524. [CrossRef]

40. Bielak, J.; Heiermann, T.; Will, N.; Hegger, J.; Raupach, M. *Zwanzig20—Carbon Concrete Composit—C3-V1.2 Nachweis- und Prüfkonzepte für Normen und Zulassungen—Schlussbericht Teilvorhaben V1.2-III 424/2019*; RWTH Aachen University: Aachen, Germany, 2019. [CrossRef]

41. Li, Y.; Bielak, J.; Hegger, J.; Chudoba, R. An incremental inverse analysis procedure for identification of bond-slip laws in composites applied to textile reinforced concrete. *Compos. Part B: Eng.* **2018**, *137*, 111–122. [CrossRef]

42. Preinstorfer, P.; Kollegger, J. Splitting Failure Mode in Textile Reinforced Concrete. In *Concrete—Innovations in Materials, Design and Structures, Proceedings of the 2019 FIB Symposium, Krakow, Poland, 27–29 May 2019*; Derkowski, W., Gwozdziewicz, P., Hojdys, L., Krajewski, P., Pantak, M., Eds.; International Federation for Structural Concrete (FIB): Cham, Switzerland, 2019; pp. 282–288. ISBN 978-2-940643-00-4.

43. Preinstorfer, P.; Kromoser, B.; Kollegger, J. Einflussparameter auf die Spaltrissbildung in Textilbeton. *Beton- und Stahlbetonbau* **2018**, *113*, 877–885. [CrossRef]

44. Lorenz, E. Endverankerung und Übergreifung Textiler Bewehrungen in Betonmatrices. Ph.D. Thesis, TU Dresden, Dresden, Germany, 2014. Available online: https://nbn-resolving.org/urn:nbn:de:bsz:14-qucosa-170583 (accessed on 5 June 2020).

45. American Society for Testing and Materials. *Standard Test. Method for Tensile Properties of Fiber Reinforced Polymer Matrix Composite Bars*; ASTM D7205/D7205M-06; ASTM International: West Conshohocken, PA, USA, 2016.

46. Schlaich, M.; Zwingmann, B.; Liu, Y.; Goller, R. Zugelemente aus CFK und ihre Verankerungen. *Bautechnik* **2012**, *89*, 841–850. [CrossRef]

47. Horvatits, J. Segmentierte Vergussverankerung für Spannglieder mit Kohlenstofffaserverbundwerkstoff. Ph.D. Thesis., Technische Universität Wien, Wien, Germany, 2008.

48. Böhm, R.; Thieme, M.; Wohlfahrt, D.; Wolz, D.; Richter, B.; Jäger, H. Reinforcement Systems for Carbon Concrete Composites Based on Low-Cost Carbon Fibers. *Fibers* **2018**, *6*, 56. [CrossRef]

49. thyssenkrupp Carbon Components GmbH. *Carbon4ReBAR. Data Sheet*; thyssenkrupp Carbon Components: Kesselsdorf, Germany, 2017.

50. Canadian Standards Association. *Design and Construction of Building Components with Fibre-Reinforced Polymers (Reaffirmed 2007)*; CSA S806-02; Canadian Standards Association: Mississauga, ON, Canada, 2007.

51. MFPA Leipzig GmbH. *Brandverhalten von Carbonbeton: Carbon Concrete Composite C³: Schlussbericht: C3-V 2.3-II*. 2019. Available online: https://doi.org/10.2314/KXP:1679084798 (accessed on 5 June 2020). [CrossRef]

52. RILEM. Bond test for reinforcement steel. 2. Pull-out test, 1983. In *RILEM Recommendations for the Testing and Use of Constructions Materials*; E & FN SPON: New York, NY, USA, 1994; pp. 218–220.

53. Schneider, K.; Butler, M.; Mechtcherine, V. Carbon Concrete Composites C3—Nachhaltige Bindemittel und Betone für die Zukunft. *Beton- und Stahlbetonbau* **2017**, *112*, 784–794. [CrossRef]

54. Deutsches Institut für Normung e.V. *Beton—Festlegung, Eigenschaften, Herstellung und Konformität; Deutsche Fassung EN 206:2013+A1:2016*; 91.100.30 (DIN EN 206:2017-01; Beuth: Berlin, Germany, 2017.

55. Triantafillou, T.C.; Papanicolaou, C.G. Shear strengthening of reinforced concrete members with textile reinforced mortar (TRM) jackets. *Mater. Struct.* **2007**, *39*, 93–103. [CrossRef]

56. Kouris, L.A.S.; Triantafillou, T.C. State-of-the-art on strengthening of masonry structures with textile reinforced mortar (TRM). *Constr. Build. Mater.* **2018**, *188*, 1221–1233. [CrossRef]

57. Deutsches Institut für Normung e.V. *Prüfverfahren für Zement-Teil 1: Bestimmung der Festigkeit. Deutsche Fassung EN 196-1:2016*; 91.100.10 (DIN EN 196-1:2016-11); Beuth: Berlin, Germany, 2016.

58. Deutsches Institut für Normung e.V. *Prüfung von Festbeton—Teil 3: Druckfestigkeit von Probekörpern. Deutsche Fassung EN 12390-3:2009*; 91.100.30 (DIN 12390-3:2009-07); Beuth: Berlin, Germany, 2009.

59. Deutsches Institut für Normung e.V. *Prüfung von Festbeton—Teil 13: Bestimmung des Elastizitätsmoduls unter Druckbelastung (Sekantenmodul). Deutsche Fassung EN 12390-13:2013*; 91.100.30 (DIN EN 12390-13:2014-06); Beuth: Berlin, Germany, 2014.

60. Schmidt, M.; Bielak, J.; Hegger, J. Large-Scale Tests on the Structural and Deformation Behaviour of I-Beams with Carbon Reinforcement. In Proceedings of the Fiber Reinforced Polymer Reinforced Concrete Structures 14, Belfast, UK, 4–7 June 2019.

61. *InfoCAD*; Version 18.00 x64; InfoGraph GmbH: Aachen, Germany, 2018.

62. Schütze, E.; Bielak, J.; Scheerer, S.; Hegger, J.; Curbach, M. Einaxialer Zugversuch für Carbonbeton mit textiler Bewehrung. *Beton- und Stahlbetonbau* **2018**, *113*, 33–47. [CrossRef]

63. Deutsches Institut für Normung e.V. *Nationaler Anhang—National Festgelegte Parameter—Eurocode 2: Bemessung und Konstruktion von Stahlbeton- und Spannbetontragwerken—Teil 1-1: Allgemeine Bemessungsregeln und Regeln für den Hochbau*; 91.010.30; 91.080.40 (DIN EN 1992-1-1/NA:2013-04); Beuth: Berlin, Germany, 2013.

64. European Committee for Standardisation. *Eurocode 2: Design of Concrete Structures—Part 1-1: General Rules and Rules for Buildings. Incl. Corrigendum 1: EN 1992-1-1:2004/AC:2008, Incl. Corrigendum 2: EN 1992-1-1:2004/AC:2010*; EN 1992-1-1:2004; European Committee for Standardisation: Brussels, Belgium, 2010.

65. Kurth, M.C. Zum Querkrafttragverhalten von Betonbauteilen mit Faserverbundkunststoff-Bewehrung. Ph.D. Thesis, RWTH Aachen University, Aachen, Germany, 2012.

66. *ABAQUS/CAE*; Version 2019 Build ID 2018_09_24-20.41.51; Dassault Systèmes SE: Velizy-Villacoublay, France, 2019.

67. Chudoba, R.; Sharei, E.; Scholzen, A. A strain-hardening microplane damage model for thin-walled textile-reinforced concrete shells, calibration procedure, and experimental validation. *Compos. Struct.* **2016**, *152*, 913–928. [CrossRef]

68. Sargin, M. Stress–Strain Relationships for Concrete and the Analysis of Structural Concrete Sections. Ph.D. Thesis, University of Waterloo, Waterloo, ON, Canada, 1971.

69. Hillerborg, A.; Modéer, M.; Petersson, P.-E. Analysis of Crack Formation and Crack Growth in Concrete by Means of Fracture Mechanics and Finite Elements. *Cem. Concr. Res.* **1976**, *6*, 773–781. [CrossRef]

70. Stoner, J.G. Finite Element Modelling of GFRP Reinforced Concrete Beams. Master's Thesis, University of Waterloo, Waterloo, ON, Canada, 2015.

71. Kueres, D.; Stark, A.; Herbrand, M.; Claßen, M. Numerische Abbildung von Beton mit einem plastischen Schädigungsmodell—Grundlegende Untersuchungen zu Normalbeton und UHPC. *Bauingenieur* **2015**, *90*, 252–264.

72. Lubliner, J.; Oliver, J.; Oller, S.; Oñate, E. A Plastic-Damage Model for Concrete. *Int. J. Solids Struct.* **1989**, *25*, 299–326. [CrossRef]

73. Bochmann, J.; Curbach, M.; Jesse, F. Carbonbeton unter einaxialer Druckbeanspruchung: Ergebnisse systematischer experimenteller Untersuchungen. *Beton- und Stahlbetonbau* **2017**, *112*, 293–302. [CrossRef]

74. Bochmann, J. Carbonbeton unter einaxialer Druckbeanspruchung. Ph.D. Thesis, TU Dresden, Dresden, Germany, 2019.

75. Bochmann, J.; Curbach, M.; Jesse, F. Carbonbeton unter Druck: Teil 2: Einfluss von Bewehrungsgeometrie und -anordnung. *Beton- und Stahlbetonbau* **2018**, *113*, 22–32. [CrossRef]

76. Branson, D.E. *Instantaneous and Time-Dependent Deflections of Simple and Continuous Reinforced Concrete Beams*; HPR Rep. No. 7, Part 1; Alabama State Highway Department: Greenville, AL, USA, 1965.

77. Bischoff, P.H.; Scanlon, A. Effective moment of intertia for calculating deflections of concrete members containing steel reinforcement and FRP reinforcement. *ACI Struct. J.* **2007**, *107*, 68–75. [CrossRef]

78. Bischoff, P.H.; Gross, S.P. Equivalent Moment of Inertia Based on Integration of Curvature. *J. Compos. Constr.* **2011**, *15*, 263–273. [CrossRef]

79. Bischoff, P.H.; Gross, S.P. Design Approach for Calculating Deflection of FRP-Reinforced Concrete. *J. Compos. Constr.* **2011**, *15*, 490–499. [CrossRef]

80. Vilanova, I.; Barris, C.; Torres, L.; Miàs, C.; Baena, M.; García, V.O. Comparative Study of Deflection Equations for FRP RC Beams. In *Advances in FRP Composites in Civil Engineering, Proceedings of the 5th International Conference on FRP Composites in Civil Engineering (CICE 2010), Beijing, China, 27–29 September 2010*; Ye, L., Feng, P., Yue, Q., Eds.; Springer: Berlin, Germany, 2010; pp. 744–747, ISBN 978-3-642-17486-5.

81. Kueres, S.; Hegger, J. Reliability analysis of footbridges pre-tensioned with carbon fiber reinforced polymer tendons under flexural loading. *Eng. Struct.* **2020**, *203*, 109546. [CrossRef]